Solar Phys (2007) 241: 99–112
DOI 10.1007/s11207-007-0291-x

Acceleration Phase of Coronal Mass Ejections: II. Synchronization of the Energy Release in the Associated Flare

Darije Maričić · Bojan Vršnak · Andrew L. Stanger · Astrid M. Veronig · Manuela Temmer · Dragan Roša

Received: 11 August 2006 / Accepted: 23 January 2007 /
Published online: 16 March 2007

Abstract We analyze the relationship between the acceleration of coronal mass ejections (CMEs) and the energy release in associated flares, employing a sample of 22 events in which the CME kinematics were measured from the pre-eruption stage up to the post-acceleration phase. The data show a distinct correlation between the duration of the acceleration phase and the duration of the associated soft X-ray (SXR) burst rise, whereas the CME peak acceleration and velocity are related to the SXR peak flux. In the majority of events the acceleration started earlier than the SXR burst, and it is usually prolonged after the SXR burst maximum. In about one half of the events the acceleration phase is very closely synchronized with the fastest growth of the SXR burst. An additional one quarter of the events may be still considered as relatively well-synchronized, whereas in the remaining quarter of the events there is a considerable mismatch. The results are interpreted in terms of

D. Maričić · D. Roša
Astronomical Observatory Zagreb, Opatička 22, 10000 Zagreb, Croatia

D. Maričić
e-mail: darije.maricic@zg.t-com.hr

D. Roša
e-mail: rosadragan@yahoo.com

B. Vršnak (✉) · M. Temmer
Hvar Observatory, Faculty of Geodesy, Zagreb, Croatia
e-mail: bvrsnak@geodet.geof.hr

M. Temmer
e-mail: mat@igam.uni-graz.at

A.L. Stanger
High Altitude Observatory, Boulder, CO, USA
e-mail: stanger@ucar.edu

A.M. Veronig
IGAM/Institute of Physics, University of Graz, Graz, Austria
e-mail: asv@igam.uni-graz.at

the feedback relationship between the CME dynamics and the reconnection process in the wake of the CME.

Keywords Coronal mass ejections · Solar flares · Reconnection

1. Introduction

Coronal mass ejections (CMEs) and solar flares are tightly related phenomena. The CME take-off is often accompanied by the so-called two-ribbon flare (sometimes also denoted as dynamical flare or eruptive flare). Such a flare is caused by the magnetic field reconnection that takes place in the wake of a CME, where the vertically stretched field lines form a vertical current sheet (*cf.* Priest, 1982).

Various observations indicate that the CME dynamics is closely related to the energy release in the associated flare, or vice versa, the energy release in the flare is tightly associated with the CME kinematics. For example, statistical studies show that CME parameters, like the velocity or kinetic energy, are correlated with characteristics of the associated flare, *e.g.*, the soft X-ray (SXR) peak flux or the integrated flux (Moon *et al.*, 2002, 2003; Burkepile *et al.*, 2004; Vršnak, Sudar, and Ruždjak, 2005). On the other hand, case studies revealed the synchronization of the SXR burst growth and the CME acceleration (*e.g.*, Kahler *et al.*, 1988; Neupert *et al.*, 2001; Zhang *et al.*, 2001; Shanmugaraju *et al.*, 2003; Maričić *et al.*, 2004; Vršnak *et al.*, 2004; Zhang *et al.*, 2004; see also Zhang and Dere, 2006, and references therein).

In this respect, it is important to note that a certain fraction of ejections are not accompanied by any significant flare energy release. Nevertheless, in such events a growing system of post-eruption loops, similar to that in two-ribbon flares (post-flare loops), is often observed (*e.g.*, Vršnak, Sudar, and Ruždjak, 2005). This implies that the magnetic field reconnection itself, rather than the flare energy release, affects the dynamics of the eruption. Indeed, measurements of the product of the flare-ribbon expansion velocity and the underlying photospheric magnetic field, representing a proxy for the coronal reconnection rate, show a close synchronization of the reconnection rate and the CME acceleration (Wang *et al.*, 2003; Qiu *et al.*, 2004; Jing *et al.*, 2005). Furthermore, the active role of reconnection is documented also by morphological changes within the erupting structure (*e.g.*, Vršnak *et al.*, 2004).

As already mentioned, a number of studies showed that the CME acceleration and the flare energy release tend to be closely synchronized. However, in most of these analyses, the results were of limited accuracy, and different sets of instruments were often used, so a comparison and systematization of results is difficult and ambiguous. In this paper, we systematize the issue of the synchronization, using a relatively large sample of events, all observed by the same set of instruments. The sample of CMEs used in this paper is the same as in the previous paper of the series (Vršnak *et al.*, 2007; hereinafter Paper I), where we analyzed the temporal and spatial scales involved in the acceleration phase.

2. Observations

The analyzed sample of events consists of 22 eruptions whose kinematics could be measured from the gradual pre-acceleration stage up to the post-acceleration stage. For the measurements of the CME kinematics we used the data recorded by the Extreme-ultraviolet Imaging

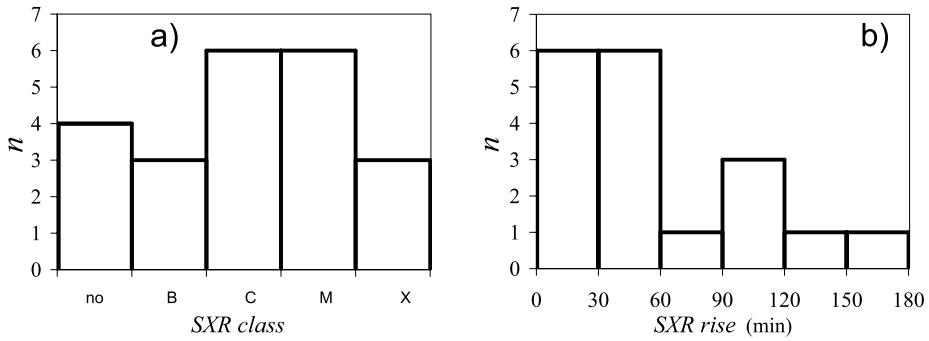

Figure 1 Distribution of: (a) GOES SXR-classes of the CME-associated flares; (b) duration of the SXR burst rise times.

Telescope (EIT; Delaboudinière *et al.*, 1995) onboard the Solar and Heliospheric Observatory (SoHO), the Solar X-ray Imager (SXI; Hill *et al.*, 2005; Pizzo, Hill, and Balch, 2005) onboard GOES, the Mark-IV K-coronameter of the Mauna Loa Solar Observatory (MLSO), and the Large Angle and Spectrometric Coronagraph (LASCO; Brueckner *et al.*, 1995) onboard SoHO (for details see Paper I). When available, the data gathered by the *Yohkoh* soft X-ray telescope (SXT, Tsuneta *et al.*, 1991) and GOES-SXI were used to check the flaring activity.

The kinematics of CMEs were traced by measuring the plane-of-sky heliocentric distance r of their leading edges (see Figure 1 of Paper I). After the measurements recorded by different instruments were superposed, a cubic-spline smoothing of the $r(t)$ data was applied (for details see Figure 2 and Appendix of Paper I). Finally, the smoothed height-time curves were employed to derive the velocity and acceleration time-profiles (for a discussion of advantages and drawbacks of such an approach see Maričić *et al.*, 2004, as well as the Appendix of Paper I).

From the velocity and acceleration time-profiles, we estimated the onset and the end of the acceleration phase (t_b and t_e, respectively), the duration of the acceleration phase ($T_{\rm acc} = t_e - t_b$), the peak velocity, $v_{\rm max}$, the time of the acceleration maximum, t_m, and the peak value of the acceleration, $a_{\rm max}$. The complete sample is displayed in Table 1, where the first three columns contain the event label, the date, and the source region location. Other relevant CME parameters (the position angle, angular width, time of the appearance in the LASCO-C2, *etc.*) can be found in Table 1 of Paper I, following the same labeling system (hereinafter, instead of using the dates, we use the event labels defined in the first column of Table 1).

In columns 4 – 6 of Table 1 we present basic kinematical properties of the CMEs: the highest speed $v_{\rm max}$ found from the smoothed velocity time-profile, the peak acceleration $a_{\rm max}$ defined by the acceleration time-profile, and the acceleration phase duration $T_{\rm acc}$. Statistical characteristics of the CME sample are presented in Paper I.

Out of the 22 eruptions analyzed in Paper I, 18 events (82%) were accompanied by a recognizable burst in the solar SXR-flux records of the GOES satellite (Donelly and Unzicker, 1974). The GOES 1 – 8 Å SXR flare classes (importances) are given in column 7 of Table 1. The distribution of the GOES classes is shown in Figure 1a (the events without a recognizable SXR increase are marked by "no").

The position of the CME source region was determined by identifying in the SOHO-EIT, *Yohkoh*-SXT, and/or GOES-SXI images the footpoints of the erupting structure (*e.g.*, a

Table 1 The list of analyzed events and their characteristics. In the last three columns we display the time lags between the beginning of the acceleration phase and the onset of the SXR burst, Dt_b, the difference between the peak acceleration and the peak of the SXR logarithmic derivative, Dt_m, and the difference between the end of the acceleration phase and the end of the SXR burst growth, Dt_e, normalized with respect to $T_{\rm acc}$. In the last two rows the average values and standard deviations are given.

Label	Date	Location	$v_{\max}$ km s^{-1}	$a_{\max}$ m s^{-2}	$T_{\rm acc}$ min	SXR class	$T_{\rm SXR}$ min	Dt_m min	$Dt_b/T_{\rm acc}$	$Dt_m/T_{\rm acc}$	$Dt_e/T_{\rm acc}$
E1	26-Feb-00	N29E50	1110	234	97	M1.0	15	2.8	−0.303	0.029	0.547
E2	28-Jun-00	N20W90	1466	1293	48	C3.7	22	−6.2	−0.200	−0.129	0.344
E3	23-Apr-01	S28W90	365	40	340	–	–	–	–	–	–
E4	15-May-01	N15E90	1224	404	140	C4.0	110	−11.2	−0.055	−0.080	0.159
E5	25-May-01	S12E90	958	300	122	–	–	–	–	–	–
E6	8-Jan-02	N53W27	480	120	144	C9.6	119	−10.9	−0.349	−0.076	−0.179
E7	9-Mar-02	S10E66	371	270	48	M1.3	30	−0.2	−0.303	−0.003	0.072
E8	6-Jun-02	N34E90	745	90	240	–	–	–	–	–	–
E9	16-Feb-03	N20W90	491	270	85	C1.4	46	21.5	0.164	0.253	0.623
E10	18-Feb-03	N65W75	802	209	155	B7.2	96	−21.5	−0.308	−0.139	0.07
E11	14-Mar-03	S20W66	881	382	57	B9.2	63	−7.8	0.026	−0.137	−0.079
E12	15-Mar-03	N07E67	629	76	295	B9.5	142	−26.6	−0.292	−0.09	0.227
E13	26-Apr-03	N16E47	705	193	152	C1.0	50	−30.5	−0.324	−0.251	0.291
E14	12-Jul-03	N16E76	412	335	23	M1.4	8	7.8	0.076	0.334	0.746
E15	15-Jul-03	N29W90	540	132	107	–	–	–	–	–	–
E16	21-Oct-03	S18E87	640	51	412	M2.4	177	−2.0	−0.171	−0.005	0.400
E17	22-Oct-03	S17E88	1143	3975	12	M9.9	20	−1.0	0.220	−0.089	−0.503
E18	26-Oct-03	N04W43	1366	1166	50	X1.2	54	−2.2	0.005	−0.044	−0.068
E19	12-Nov-03	S05W80	940	363	61	C3.2	41	12.1	0.065	0.197	0.385
E20	18-Aug-04	S12W88	740	766	40	X1.8	11	12.1	−0.062	0.303	0.672
E21	17-Jan-05A	N14W23	2084	423	127	M6	43	17.1	−0.433	0.135	0.226
E22	17-Jan-05B	N14W23	2775	7316	13	X3.8	12	−2.2	−0.279	−0.164	−0.190
Average			948	836	126	M5.1	59	−2.7	−0.14	−0.002	0.208
Stdev			560	1670	108		50	14.3	0.198	0.171	0.334

filament and/or the overlying arcade), flare or flare-like brightenings, coronal dimming, and post-eruption loop system. In the majority of events most of these features were present. In five events (E4, E5, E8, E9, and E15), the footpoints of the erupting structure were partly behind the limb. Two of these, E5 and E8, belong to the subset of four events showing no recognizable SXR enhancement. In all events we checked also if some simultaneous flaring activity was taking place at other parts of the solar disc. Indeed, in some cases such (roughly) simultaneous activity was present, but still it was possible to identify the appropriate signal in GOES records, since there was always some lag between the bursts (see the discussion of E6 and E12 in Section 3.2).

For the analysis of the synchronization of the CME acceleration and the flare energy release, we used the rising phase of the SXR burst as a proxy that outlines the flare impulsive phase. This way of identifying the impulsive phase is based on the so-called Neupert effect (Neupert, 1968; see also Veronig *et al.*, 2002, and references therein), according to which the hard X-ray or microwave burst light-curves approximately correspond to the derivative of

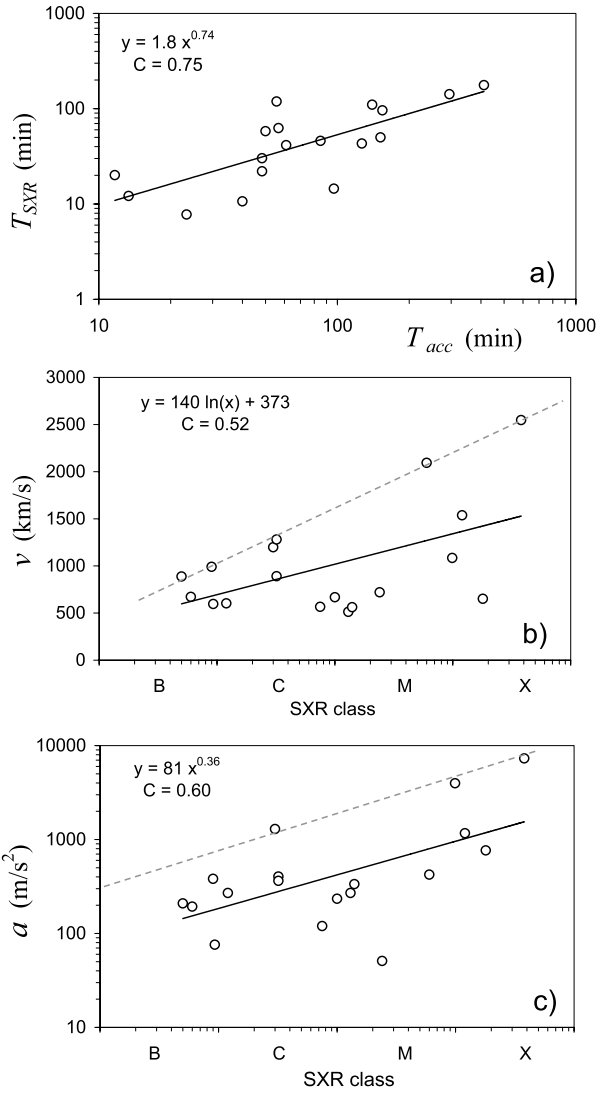

Figure 2 (a) The SXR burst rise time shown as a function of the acceleration phase duration; (b) CME mean velocities shown as a function of the SXR burst peak-flux; (c) CME peak accelerations shown as a function of the SXR-class. In (b) and (c) the background SXR level measured at the flare onset is subtracted. Dashed lines in (b) and (c) represent a provisionally determined upper limit. In the insets, the linear least squares fits are shown, together with correlation coefficients, C. Correlations in (a) and (c) have the F-test statistical significance larger than 99%, whereas the correlation in (b) has the significance larger than 92%.

the SXR light-curve. In particular, we employed the SXR light-curves recorded in the $1-8$ Å and $0.5-4$ Å GOES channels. The 3-second resolution GOES data were smoothed by the cubic spline procedure, and from the smoothed light curve $f(t)$ we calculated the "ordinary" derivative, $\mathrm{d}f/\mathrm{d}t$, as well as the logarithmic derivative $\mathrm{d}(\log f)/\mathrm{d}t = f^{-1}\,\mathrm{d}f/\mathrm{d}t$.

The basic difference between the two derivatives lies in the fact that the logarithmic derivative measures the rate of growth normalized to the current value of the SXR flux. So, it represents relative increment of the SXR flux, whereas the ordinary derivative measures the absolute increment. Note that the two derivatives could show considerable differences, leading to different conclusions (compare, *e.g.*, logarithmic light-curves and ordinary derivatives in Figures 2 – 7 of Kim *et al.*, 2005, and check the corresponding text). In the analysis we considered both options, but in following we present only the results concerning the SXR

logarithmic derivatives, since it turned out that on average they show a better match with the acceleration time profiles than the ordinary derivatives.

From the logarithmic light curves we determined the times of the burst onset and maximum, as well as the peak of the logarithmic derivative (the fastest rise of the logarithmic light-curve). The former two parameters are used to evaluate the SXR burst rise time T_{SXR}. The T_{SXR} data are presented in column 8 of Table 1, and their distribution is shown in Figure 1b. On average, the rise-time lasted around 1 hour, *i.e.*, the associated flares were generally long duration events. Only E14 was of a somewhat shorter duration, since the SXR rise to the M1.4 level lasted 8 minutes, and the flux decayed to 1/2 of the peak value in about 20 minutes.

From the obtained data, we derived the time differences between the beginning of the acceleration phase and the onset of the SXR burst, Dt_b, the difference between the peak acceleration and the peak of the SXR logarithmic derivative, Dt_m, and the difference between the end of the acceleration phase and the end of the SXR burst growth (*i.e.*, the SXR peak), Dt_e. The time difference Dt_m between the peak acceleration and the peak of the SXR flux derivative (the fastest rise of the SXR burst) is presented in column 9 of Table 1.

Since the time differences and the related errors obviously depend on the duration of the event itself, we also employ the normalized time differences, where we divide a given delay by the acceleration phase duration. The normalized delays Dt_b/T_{acc}, Dt_m/T_{acc}, and Dt_e/T_{acc} are presented in columns 10 – 12 of Table 1.

3. Results

3.1. Statistical Correlations

In Figure 2a we present the relationship between the duration of the acceleration phase and the rise-time of the SXR burst. The graph shows a distinct correlation between these two parameters, characterized by the correlation coefficient $C = 0.75$. The F-test statistical significance is larger than 99.99% (the significance $P > 99.99\%$ implies the probability of no correlation between two parameters is less than 0.01%).

In Figures 2b and c we show two more aspects of the relationship between the CME kinematics and the SXR burst. The graphs show that CMEs of larger speeds and accelerations on average are associated with more powerful flares (see also Moon *et al.*, 2002; Moon *et al.*, 2003; Burkepile *et al.*, 2004; Vršnak, Sudar, and Ruždjak, 2005). However, a strong SXR burst is not necessarily associated with a high-speed or high-acceleration CME — there are events populating the lower-right part of the graphs. On the other hand, there is apparently an upper limit on the CME velocity and acceleration, related to the SXR burst peak flux. We depicted provisionally this upper limit by the dashed line in Figures 2b and c, to separate the empty upper-left part of the graph from the populated lower-right part. However, one has to bear in mind that our sample is relatively small, so adding more events could change the situation considerably (for a discussion see Figure 3d of Vršnak, Sudar, and Ruždjak, 2005).

3.2. Synchronization of the CME Acceleration and the SXR Burst

Inspecting column 9 of Table 1 one finds that the acceleration peaks in the majority of events are closely associated with the fastest growth of SXR bursts. The distribution of delays Dt_m presented in Figure 3 peaks at $Dt = 0$ and shows a slightly asymmetric shape. The distribution is characterized by $Dt_m = -2.7 \pm 14$ min. Inspecting column 11 of Table 1, where

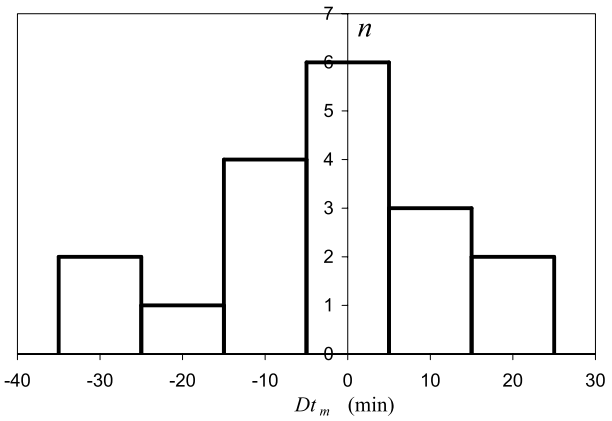

Figure 3 Distribution of the time difference between the acceleration peak and the peak of the SXR flux derivative (the fastest rise of the SXR burst).

the normalized time difference $Dt_m/T_{\rm acc}$ is presented, one finds that the peak acceleration and the peak of the 1 – 8 Å SXR burst derivative are synchronized to within 1/3 of the duration of the acceleration phase. Bearing in mind the accuracy of the measurements and the data reduction procedure, we consider such a behavior as an outstanding synchronization. However, one should bear in mind that the time difference in several events is larger than 20 minutes.

The scatter is somewhat larger if the time differences between the onset of the acceleration phase and the onset of SXR burst are considered, or if the end of the acceleration phase is compared with the end of the SXR burst growth (*i.e.*, the SXR peak). That is not surprising, since determining the onset and the end times is more ambiguous than the estimate of peak times. Nevertheless, the average values again show a quite systematic behavior. In most events, the SXR burst onset is delayed after the onset of the acceleration (on average $Dt_b = -23 \pm 30$ min), whereas the acceleration ends after the SXR burst had already reached its maximum ($Dt_e = 27 \pm 43$ min).

In order to eliminate the effect of different time scales involved (events of longer duration show larger time differences), we normalized the delays by dividing them with the duration of the acceleration phase. Inspecting column 11 of Table 1, one finds that the normalized time differences between the peak acceleration and the peak of the SXR derivative, $Dt_m/T_{\rm acc}$, range from -0.25 to $+0.33$ (negative values mean that the acceleration peaks before the SXR derivative), whereas the mean value amounts to only -0.002. The time differences concerning the acceleration phase onset and the SXR burst start, $Dt_b/T_{\rm acc}$, and the end of the acceleration phase and the end of the SXR rise, $Dt_e/T_{\rm acc}$, are somewhat larger (see columns 10 and 12 of Table 1).

The distributions of the delays Dt_b, Dt_m, and Dt_e, normalized with respect to $T_{\rm acc}$, are shown in Figures 4a – c, respectively. The distributions are characterized by the mean values $Dt_b/T_{\rm acc} = -0.14 \pm 0.20$, $Dt_m/T_{\rm acc} = -0.002 \pm 0.17$, and $Dt_e/T_{\rm acc} = 0.21 \pm 0.33$, clearly showing a close synchronization of the acceleration phase and the growth of the SXR burst. In Figure 5 we show the relative timing of the acceleration phase and the SXR burst growth for each event separately, where the times are normalized by the duration of the acceleration phase ($t_b^* = 0$; $t_e^* = 1$). On average (see Figure 4), and in the majority of the events (see Figure 5), the acceleration starts before the SXR burst, and extends after the end of the SXR burst rise. The mean value of $|Dt_m/T_{\rm acc}|$ equals to 0.14, *i.e.*, the time lag between the acceleration peak and steepest rise of SXR burst, on average amounts to 14% of the acceleration phase duration.

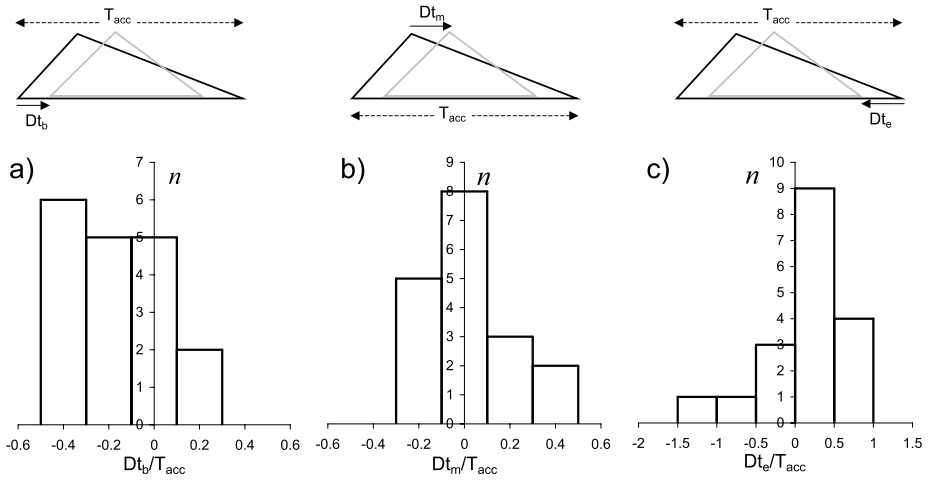

Figure 4 Distribution of normalized time differences between: (a) beginning of the acceleration phase and the beginning of the 1 – 8 Å SXR burst; (b) the acceleration peak and the peak of the SXR flux logarithmic derivative; (c) the end of the acceleration phase and the end of SXR burst growth. Note the different x-axis scale in (c). The schematic drawings above the histograms define the used symbols (black triangles represent the acceleration time profile, gray triangles depict the profile of the SXR burst logarithmic derivative, the right-arrow means $Dt < 0$, the left-arrow means $Dt > 0$).

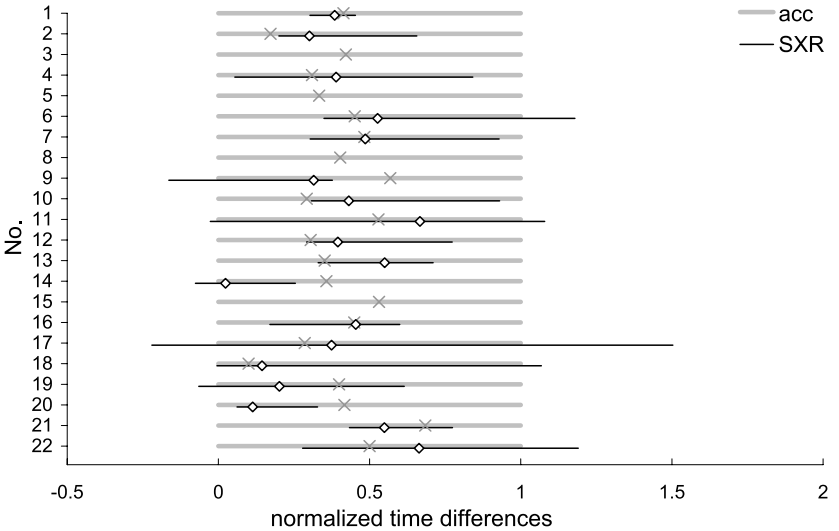

Figure 5 Synchronization of the CME acceleration phase (gray; duration normalized to $Dt^*_{\rm acc} = 1$) and the energy release in the associated flare (black; appropriately normalized phase of the SXR burst growth). Gray crosses mark the acceleration peak, black diamonds the fastest growth of the 1 – 8 Å SXR burst (peak of the SXR flux logarithmic derivative).

In Figures 6a – d we show the CME acceleration, SXR logarithmic light-curve $F(t)$, and the SXR logarithmic derivative in four events, to illustrate various modalities of the

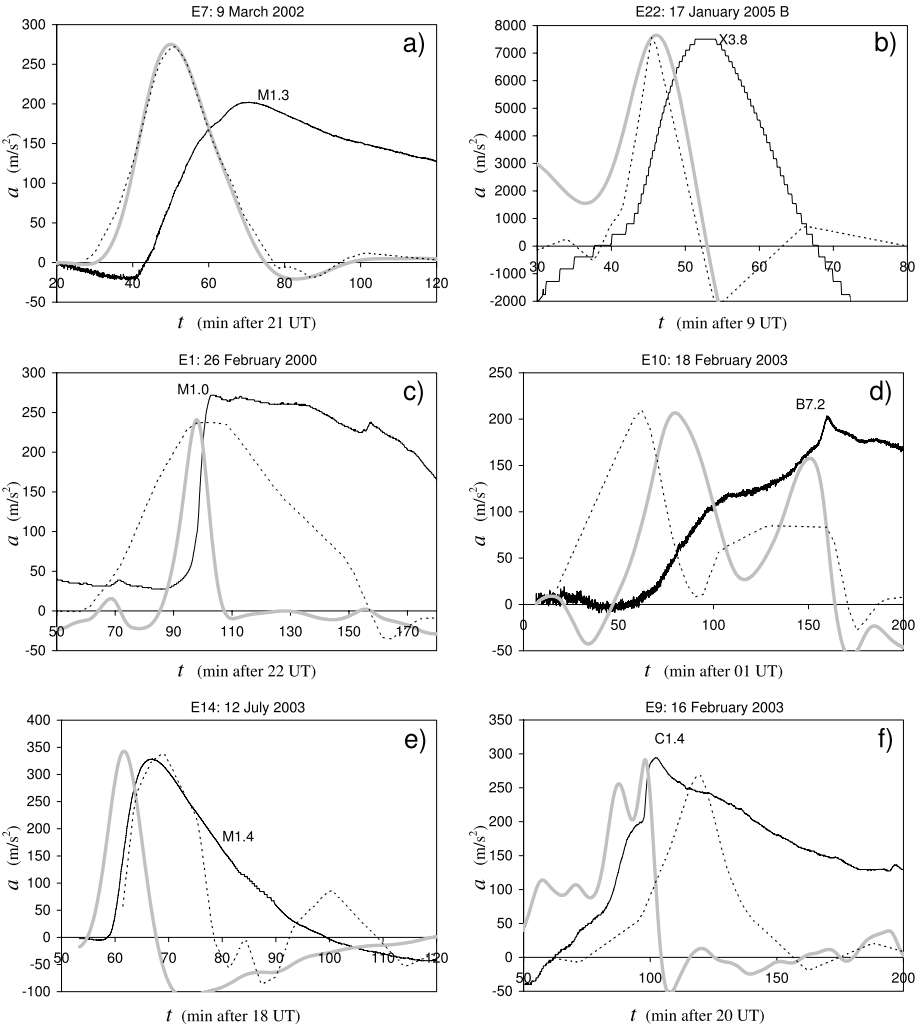

Figure 6 (a) – (f) The smoothed CME acceleration (dashed), the SXR 1 – 8 Å logarithmic light-curve (thin-black; peak flux is indicated by the curve), and the logarithmic derivative of the SXR light-curve (bold-gray). Events E7, E22, E1, E10, E14, and E9, are shown respectively (dates are written at the top of the graphs). The SXR light curves and their derivatives are given in arbitrary units (adjusted to be comparable with the acceleration curves). The events in (a) and (b) show an almost perfect match of the acceleration curve and the SXR derivative. In (c) and (d), we show two events which we consider as "synchronized", but the relationship is not that good as in (a) and (b). In (e) and (f) we show two "mismatch events": in (e) the acceleration curve overlaps with the SXR light-curve instead of overlapping with its derivative; in (f) the acceleration peaks after the peak of the SXR burst.

synchronization. The events presented in Figures 6a and b (E7 and E22, respectively) exhibit an almost perfect match of the acceleration time-profile and the logarithmic derivative of the SXR flux, very similar to that found by Maričić *et al.* (2004) in E4. Note that E22 (Figure 6b) showed an extremely impulsive acceleration, with the peak value larger than 7000 m s^{-2}.

The category of tightly synchronized CME-flare events includes also E2, E6, E11, E12, E16, and E18, although the SXR flux derivative is somewhat more complex in these events, showing 2 – 3 maxima. Here, it is instructive to describe in more detail the situation in E6 and E12, since this kind of the SXR/acceleration pattern might lead to incorrect conclusions. In both events, SXR bursts were recorded approximately at the time of the acceleration phase, yet they showed a significant mismatch. However, the dominant SXR bursts were caused by remote flares, *i.e.*, they were not associated with the considered CMEs. On the other hand, inspecting the SXR recordings, we found a weaker SXR bursts whose rise-phases were well-synchronized with the CME acceleration phase. So, altogether, in nine out of 18 events that showed a distinct SXR burst (50%), the CME acceleration phase was strongly correlated with the growth of the SXR burst. It is also worth mentioning that E16 showed a complex CME activity, consisting of multiple ejections in the LASCO-C2 field of view: the measured ejection which entered into the LASCO-C2 field of view at 19:54 UT was followed by ejections at 20:58 and 23:30 UT.

In the events E1, E10, E13, E17, and E21 (5 out of 18; 28%) the acceleration phase and the SXR burst growth were synchronized to a certain degree, but not as well as in the previous group of events. We illustrate this category in Figures 6c and d, where we show the events E1 and E10. The former one shows simultaneity of the acceleration maximum and the peak of the SXR flux derivative (Figure 6c), but the acceleration phase lasted approximately five times longer than the SXR flux growth. In other words, the SXR growth was much more impulsive than the CME acceleration. In the latter case we find that the acceleration starts considerably earlier than the SXR burst. On the other hand, Figure 6d shows that in E10, there were two acceleration peaks and two phases of the SXR burst growth. So, although the synchronization is not perfect, we take this to be an evidence of the correlation of the flare energy release and the CME acceleration.

In the remaining four events (E9, E14, E19, and E20), representing 22% of the sample, there was a considerable mismatch between the acceleration phase and the phase of the SXR burst growth. We illustrate the degree of mismatch in Figures 6e and f, where we show the events E14 and E9. In the former case, the acceleration time-profile is closely matching to the SXR light-curve itself, *i.e.*, it shows a pattern basically different from previous cases. A similar pattern is found also in E19 and E20.[1] A still larger mismatch than in the three mentioned events is found in E9 (Figure 6f), where the acceleration starts more than half an hour after the onset of the SXR burst and peaks more than ten minutes after the SXR burst maximum.

A separate category of events is represented by E5, E8, and E15, whose source region was only partly at the visible hemisphere, and there was no recognizable flare activity or SXR enhancement associated with the eruption. However, it is important to note that even in these three events a growing system of post-eruption loops was observed, revealing the ongoing reconnection in the wake of the CME.

Finally, we note that the complete procedure was repeated by employing the GOES 0.5 – 4 Å SXR measurements as well, and we found a very similar outcome: in the majority of events, the acceleration peak is synchronized with the fastest growth of the SXR burst. The only difference is in a slight shift of the distributions, since the 0.5 – 4 Å SXR bursts generally peak few minutes earlier than the 1 – 8 Å burst. For example, on average the acceleration peak is delayed after the peak of the logarithmic derivative of the 0.5 – 4 Å SXR light-curve

[1]Note that an analogous situation is also found in a certain fraction of SXR plasmoid-ejections analyzed by Kim *et al.* (2005).

for 0.6 ± 14 minutes (*i.e.*, on average the $0.5-4$ Å derivative peaks $0.6 + 2.7 = 3.3$ minutes earlier than the $1-8$ Å burst).

4. Discussion and Conclusion

We summarize the results of our analysis as follows:

1. In the majority of events the acceleration starts earlier than the SXR burst, and it is usually prolonged after the SXR burst maximum;
2. In about half of the events the acceleration phase is very closely synchronized with the growth of the SXR burst. In addition, roughly one quarter of the sample can still be considered as relatively well-synchronized;
3. In the remaining one quarter of the events, a considerable mismatch was found;
4. There is a distinct correlation between the duration of the acceleration phase and the duration of the SXR burst rise;
5. In all events (including four non-SXR events whose source region was only partly on the visible hemisphere), a growing system of post-eruption (post-flare) loops was observed.

Summary item 1 implies that the eruption generally starts earlier than the flare energy release, evidencing that dynamical flares occur as a consequence of the eruption. Furthermore, since signatures of dissipative processes (heating and particle acceleration) are absent in the early stages of the eruption, we conclude that the eruption is initially driven by ideal MHD processes.

However, there are events where the acceleration starts after the onset of the associated flare (*e.g.*, E9 and E17). In this respect we also have to describe in more details the situation in E13, where we found two (very weak) SXR bursts, both associated with the CME source region. The first one appeared at the very onset of the acceleration phase, which was in this event quite gradual ($T_{\rm acc} > 2.5$ hours). This first burst ceased much before the acceleration peak (not shown in Table 1 and Figure 5). On the other hand, the second SXR burst (data displayed in Table 1 and Figure 5) showed a relatively good synchronization with the acceleration phase.

A possible explanation for the SXR/acceleration pattern observed in E9 and E17, and particularly in E13, is that in the pre-eruption stage a confined type of flare develops. It may be presumed that this confined flare releases only a part of the energy stored in the pre-erupting structure. However, the associated magnetic field restructuring might transform the stable structure into the unstable one, providing its immediate eruption (for a discussion see, *e.g.*, Low, 1996). Only then, after the eruption onset, the standard two-ribbon flare takes place, although in the SXR curve, it might look just as a prolongation of the first flare.

Such a fast pre-eruption magnetic field restructuring caused by a compact flare could be considered as a tether-cutting type of process (Moore, LaRosa, and Orwig, 1995), or as a process that forms an unstable, helically twisted structure (Vršnak, 2003). This kind of development, characterized by an abrupt transition to the instability, is considerably different from the loss of equilibrium during a gradual evolution of the system through a series of equilibrium states. Unfortunately, in the case of the mentioned events E9, E13, and E17, we do not have a direct observational support for such a scenario. Since only the EIT data were available (cadence of 12 minutes only), we could not perform an adequate analysis of the flare development.

Considering the eruption itself, our measurements show that in the majority of events the acceleration peak is associated with the fastest growth of the SXR burst (column 10

of Table 1 and Figure 5). That indicates either: (i) the reconnection becomes the dominant component in the dynamics of the eruption, *i.e.*, resistive processes take over; (ii) the reconnection rate is determined by the CME kinematics; or (iii) a feedback relationship between the CME kinematics and the reconnection process is established after the initial stage of the eruption. A tight synchronization of the CME acceleration and the flare energy release (summary items 2 and 4) indicates that the feed-back relationship between the CME dynamics and the reconnection process is probably established in a certain number of events.

The reconnection process has two important effects on the CME. Firstly, the reconnection reduces the net tension of the overlying arcade field and increases the magnetic pressure below the flux-rope, which is certainly playing a significant role for the CME dynamics (*e.g.*, Van Tend and Kuperus, 1978; Anzer and Pneuman, 1982; Forbes, 1990; Lin, 2002). Secondly, the upward-directed reconnection jet carries the reconnected field lines to the erupting flux-rope, supplying it with a "fresh" poloidal flux. This effect enhances the "hoop" force (*e.g.*, Mouschovias and Poland, 1978; Chen, 1989; Vršnak, 1990; Chen and Krall, 2003), thus enhancing and prolonging the flux-rope acceleration (Vršnak, 1990). On the other hand, the CME expansion determines the overall geometry of the system and the flows behind the flux-rope, both of which affect the reconnection process (Vršnak and Skender, 2005). In this way, a feedback relationship between the CME motion and the flare energy release is established. The synchronization of the CME acceleration and the energy release in the flare is most likely a consequence of such a feed-back, since the reconnection rate determines also the energy release in the flare. However, the weakly-synchronized and mismatch events (summary item 3) indicate that such a feedback is not necessarily the dominant effect in the CME take-off.

Considering the end of the CME acceleration, we found that the acceleration most often continues after the SXR burst has attained its maximum (column 12 of Table 1 and Figure 5). This may be explained by the weakening of the energy release in the late phase of a long-duration flare, when it becomes too weak to compensate cooling of the hot flare plasma. In such a case the rising phase of the SXR burst is not a reliable proxy to determine the flare impulsive phase, since the SXR flux starts to decrease although the energy release did not finish yet (for departures from the Neupert effect see, *e.g.*, Dennis and Zarro, 1993; Veronig *et al.*, 2002, and references therein). The ongoing reconnection is evidenced by growing post-eruption loop system (summary item 5) which can last for hours (*e.g.*, Vršnak *et al.*, 2004).

Finally, bearing in mind also the results presented in Paper I, we can conclude that CMEs of small initial size (called in Paper I "compact CMEs") that are launched from active regions, tend to have an impulsive acceleration, especially if associated with a powerful flare (Figure 2c). The CMEs of large source sizes, launched from "quiet" solar regions, develop more gradually and are associated with weaker flares. That is not surprising, since the magnetic field in active regions is strong, especially at low heights. Consequently, the Lorentz force is stronger (larger acceleration), the Alfvén speed is higher (shorter time scales involved), and the energy release associated with the reconnection is more powerful (stronger flare).

In this respect, we emphasize that we find no evidence of two distinct classes of CMEs, *i.e.*, the flare-associated class and the non-flare class (for an extended discussion see Vršnak, Sudar, and Ruždjak, 2005). Rather, we found that there is a continuous spectrum of accelerations, which shows only a statistical tendency of stronger accelerations being associated with more powerful flares. Moreover, Figure 2b shows that some CMEs associated with X-class flares have velocities comparable to CMEs associated with B-class flares.

Such a pattern indicates that the flare energy release itself is not the dominant factor that determines the CME acceleration. More likely, the relevant parameter is the reconnection rate: an efficient reconnection gives rise to a fast CME acceleration, but not necessarily also a strong heating and non-thermal particle acceleration. This is expected to happen in regions of comparatively large plasma-to-magnetic pressure ratio, say, $\beta > 0.1$ (Vršnak and Skender, 2005). Such a condition is more likely to be found outside of active regions and at larger heights, *i.e.*, in the case of CMEs associated with quiescent filament eruptions. On the other hand, in the efficient-reconnection events (evidenced by a powerful flare), the CME acceleration can be suppressed if the pre-erupting structure contains a large amount of mass (large inertia), or if it is overlain by a large magnetic flux. The latter effect might even prevent the eruption ("failed eruptions"; see, *e.g.*, Török and Kliem, 2005, and references therein).

Acknowledgements This work is sponsored by the Air Force Office of Scientific Research, USAF, under grant number FA8655-06-1-3036. M.T. and A.V. acknowledge the support by the Austrian Science Fund (FWF grant P15344 and J2512-N02). We are grateful to the GOES, MLSO, and SOHO teams for developing and operating the instruments and we appreciate their open data policies. We are thankful to Nariaki Nitta, and Werner M. Neupert for constructive comments and suggestions which led to a significant improvement of the paper.

References

Anzer, U., Pneuman, G.W.: 1982, *Solar Phys.* **79**, 129.
Brueckner, G.E., Howard, R.A., Koomen, M.J., *et al.*: 1995, *Solar Phys.* **162**, 357.
Burkepile, J.T., Hundhausen, A.J., Stanger, A.L., St. Cyr, O.C., Seiden, J.A.: 2004, *J. Geophys. Res.* **109**, A03103, doi:10.1029/2003JA010149.
Chen, J.: 1989, *Astrophys. J.* **338**, 453.
Chen, J., Krall, J.: 2003, *J. Geophys. Res.* **108**(A11), 1410, doi:10.1029/2003JA009849.
Delaboudinière, J.-P., Artzner, G.E., Brunaud, J., *et al.*: 1995, *Solar Phys.* **162**, 291.
Dennis, B.R., Zarro, D.M.: 1993, *Solar Phys.* **146**, 177.
Donelly, B.R., Unzicker, A.: 1974, NOAA Tech. Memo ELR SEL-72.
Forbes, T.G.: 1990, *J. Geophys. Res.* **95**, 11919.
Hill, S.M., Pizzo, V.J., Balch, C.C., *et al.*: 2005, *Solar Phys.* **226**, 255.
Jing, J., Qiu, J., Lin, J., Qu, M., Xu, Y., Wang, H.: 2005, *Astrophys. J.* **620**, 1085.
Kahler, S.W., Moore, R.L., Kane, S.R., Zirin, H.: 1988, *Astrophys. J.* **328**, 824.
Kim, Y.-H., Moon, Y.-J., Cho, K.-S., Bong, S.-C., Park, Y.D.: 2005, *Astrophys. J.* **635**, 1291.
Lin, J.: 2002, *Chin. J. Astron. Astrophys.* **2**, 539.
Low, B.C.: 1996, *Solar Phys.* **167**, 217.
Moon, Y.-J., Choe, G.S., Wang, H., Park, Y.D., Gopalswamy, N., Yang, G., Yashiro, S.: 2002, *Astrophys. J.* **581**, 694.
Moon, Y.-J., Choe, G.S., Wang, H., Park, Y.D., Cheng, C.Z.: 2003, *J. Korean Astron. Soc.* **36**, 61.
Maričić, D., Vršnak, B., Stanger, A.L., Veronig, A.: 2004, *Solar Phys.* **225**, 337.
Moore, R.L., LaRosa, T.N., Orwig, L.E.: 1995, *Astrophys. J.* **438**, 985.
Mouschovias, T.Ch., Poland, A.I.: 1978, *Astrophys. J.* **220**, 675.
Neupert, W.M., 1968, *Astrophys. J.* **153**, L59.
Neupert, W.M., Thompson, B.J., Gurman, J.B., Plunkett, S.P.: 2001, *J. Geophys. Res.* **106**, 25215.
Pizzo, V.J., Hill, S.M., Balch, C.C., *et al.*: 2005, *Solar Phys.* **226**, 283.
Priest, E.R.: 1982, *Solar Magnetohydrodynamics*, Reidel, Dordrecht.
Qiu, J., Wang, H., Cheng, C.Z., Gary, D.E.: 2004, *Astrophys. J.* **604**, 900.
Shanmugaraju, A., Moon, Y.-J., Dryer, M., Umapathy, S.: 2003, *Solar Phys.* **215**, 185.
Török, T., Kliem, B.: 2005, *Astrophys. J.* **630**, L97.
Tsuneta, S., Acton, L., Bruner, M., *et al.*: 1991, *Solar Phys.* **136**, 37.
Van Tend, W., Kuperus, M.: 1978, *Solar Phys.* **59**, 115.
Veronig, A., Vršnak, B., Dennis, B.R., Temmer, M., Hanslmeier, A., Magdalenić, J.: 2002, *Astron. Astrophys.* **392**, 699.
Vršnak, B.: 1990, *Solar Phys.* **129**, 295.

Vršnak, B.: 2003, In: Klein, K.-L. (ed.) *Energy Conversion and Particle Acceleration in the Solar Corona*, *Lect. Notes Phys.* **612**, 28.
Vršnak, B., Skender, M.: 2005, *Solar Phys.* **226**, 97.
Vršnak, B., Maričić, D., Stanger, A.L., Veronig, A.: 2004, *Solar Phys.* **225**, 355.
Vršnak, B., Sudar, D., Ruždjak, D.: 2005, *Astron. Astrophys.* **435**, 1149.
Vršnak, B., Maričić, D., Stanger, A.L., Veronig, A., Temmer, M., Roša, D.: 2007, *Solar Phys.* **241**, 87.
Wang, H., Qiu, J., Ju, J., Zhang, H.: 2003, *Astrophys. J.* **593**, 564.
Zhang, J., Dere, K.P.: 2006, *Astrophys. J.* **649**, 1100.
Zhang, J., Dere, K.P., Howard, R.A., Kundu, M.R., White, S.M.: 2001, *Astrophys. J.* **559**, 452.
Zhang, J., Dere, K.P., Howard, R.A., Vourlidas, A.: 2004, *Astrophys. J.* **604**, 420.